Journal of Molecular Graphics and Modelling 30 (2011) 1–9

Contents lists available at ScienceDirect

Journal of Molecular Graphics and Modelling

journal homepage: www.elsevier.com/locate/JMGM

Computational insights into the different catalytic activities of CYP2A13 and CYP2A6 on NNK

You Xu, Zhonghua Shen, Jie Shen, Guixia Liu, Weihua Li*, Yun Tang*

Department of Pharmaceutical Sciences, School of Pharmacy, East China University of Science and Technology, 130 Meilong Road, Shanghai 200237, China

ARTICLE INFO

Article history:
Received 31 March 2011
Received in revised form 18 May 2011
Accepted 19 May 2011
Available online 27 May 2011

Keywords:
CYP2A13
CYP2A6
NNK
Molecular dynamics
Molecular docking

ABSTRACT

The human cytochrome P450 2A13 (CYP2A13) and P450 2A6 (CYP2A6) are 94% identical in amino acid sequence, but they metabolize many substrates with different efficiencies. Previous experimental results have shown that CYP2A13 exhibited catalytic activity that was more than 300-fold higher than CYP2A6 toward 4-(methylnitrosamino)-1-(3-pyridyl)-1-butanone (NNK), a carcinogen present in tobacco products. At present, however, the structural determinants accounting for the differential catalytic activities of these two isozymes toward NNK remain unclear. In the present study, molecular docking combined with molecular dynamics simulation and binding free energy calculation was performed to investigate the above issue. The results demonstrate that NNK was able to form a hydrogen bond with Asn297 in either CYP2A13 or CYP2A6. The hydrogen-bond acceptor was the pyridine nitrogen of NNK in the CYP2A13 complex, but it changed to the carbonyl oxygen in the CYP2A6 complex. NNK interacted with the residues in helix I and the K-β2 loop in CYP2A13, whereas it preferred to contact with the phenylalanine cluster in CYP2A6. The residues in helix I and the K-β2 loop of CYP2A13 played a vital role in keeping NNK in a more stable binding state. The binding free energies calculated by MM-GBSA were in agreement with the experimental results.

1. Introduction

The human cytochrome P450s (CYPs) are a superfamily of heme-containing monooxygenases that catalyze a large number of oxidative reactions by a hydroxylation process. They are mainly located in the inner membrane of mitochondria or in the endoplasmic reticulum of cells. These enzymes play an important role in the metabolic activation and detoxification of a large number of exogenous and endogenous compounds. CYP2A6 and CYP2A13 belong to the CYP2A subfamily and are responsible for the metabolism of diverse xenobiotics, such as drugs, carcinogens, and environmental contaminants [1]. CYP2A6 mainly exists in the liver, whereas CYP2A13 is present in the respiratory tract and at low levels in the liver [2,3].

4-(Methylnitrosamino)-1-(3-pyridyl)-1-butanone (NNK), a nitrosated derivative of nicotine, is a carcinogen in tobacco products. It is produced from tobacco processing and cigarette smoking and plays an important role in human tobacco-related cancers [4]. Both CYP2A6 and CYP2A13 can activate NNK via hydroxylation at the methylene (C9) or methyl carbon (C10). The former is further hydrolyzed to 4-oxo-1-(3-pyridyl)-1-butanone (OPB) and methane diazohydroxide, and the latter produces 4-hydroxy-1-(3-pyridyl)-1-butanone (HPB) [4,5] (Fig. 1a). These metabolites eventually turn into DNA adducts, which induce lung cancer [6].

As a hepatic enzyme, CYP2A6 was considered to be the most efficient CYP for NNK metabolism [7,8]. However, subsequent studies suggested that CYP2A13 in the respiratory tract had a higher efficiency for NNK activation [9,10]. Previous experimental data has shown that CYP2A13 catalyzes NNK with a K_m that is 20–60 times lower and a V_{max}/K_m more than 300 times higher than CYP2A6 [7,9–11]. In addition to NNK, CYP2A13 and CYP2A6 also exhibited distinct metabolism kinetic profiles toward other common substrates [1,9,12–14]. These two isozymes have the same amino acid sequence length (494 residues), and only 32 residues differ in their corresponding alignment positions. Therefore, the mechanisms through which they exhibit differential catalytic activities toward common substrates are of particular interest.

Recently, the crystal structures of CYP2A13 and CYP2A6 have been resolved [15–17]. Not surprisingly, the two structures display a high similarity at the gross level because of their high sequence identity. The root-mean-square deviation (RMSD) of Cα atoms in the two structures is only 0.5 Å. However, the structural superposition also reveals differences in some local sites, especially around the active site. For instance, 10 of the 32 non-identical residues are located in or near the binding site and were considered to be potential contributors to their differential catalytic activities

* Corresponding authors. Tel.: +86 21 64251052; fax: +86 21 64253651.
E-mail addresses: whli@ecust.edu.cn (W. Li), ytang234@ecust.edu.cn (Y. Tang).

1093-3263/$ – see front matter © 2011 Elsevier Inc. All rights reserved.
doi:10.1016/j.jmgm.2011.05.002

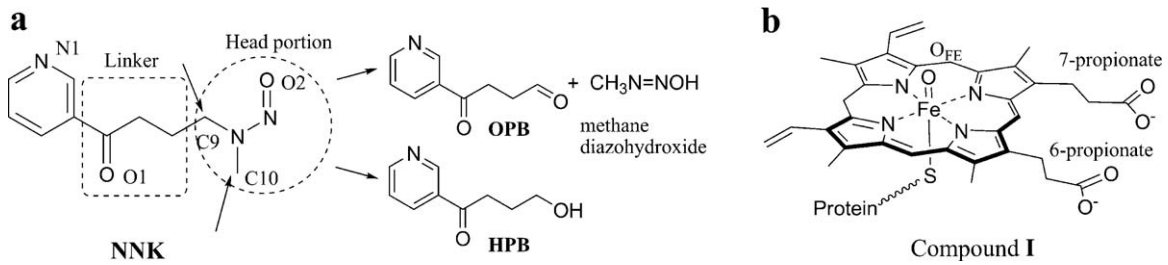

Fig. 1. (a) Chemical structure of NNK with partial atom number and structure labeling. Arrows indicate the positions of hydroxylated carbon, and the metabolites are corresponding to the two hydroxylated positions respectively. (b) Chemical structure of heme-thiolate complex with oxygen O_{FE} (compound **I**).

on common substrates. Previous site-directed mutagenesis results demonstrated that these two enzymes have remarkable differences in catalytic activities toward some substrates after exchanging some of the non-identical residues [18–20]. He et al. also found that several residues around the active site of CYP2A13 were critical for the metabolic activation of NNK [21]. Nevertheless, the issue of how these residues affect the binding of NNK and thus cause the differential catalytic activities between the two CYP2A isozymes remains elusive.

To shed light on this issue, molecular docking combined with molecular dynamics (MD) simulations and free energy calculations was carried out on CYP2A13 and CYP2A6. The initial CYP2A–NNK complex models were obtained using molecular docking. The favorable positions from the docking results were selected as the starting structures for MD simulations, and the binding free energy calculations and free energy decomposition were performed based on the MD results. Our results indicate that Asn297 guides the orientation of NNK in the active sites, and the hydrophobic interactions stabilize the substrate binding in both CYP2A13 and CYP2A6. Among them, several non-identical residues in the two CYPs made the shape of binding site different, which led to differences in the NNK binding modes.

2. Methods

2.1. Protein preparation

All the protein structures used in this study were taken from the Protein Data Bank (PDB). To date, only one structure is available for CYP2A13 (PDB ID: 2P85) [15]. This is a complex bound with indole, which contains 6 chains. For CYP2A6, more than ten structures, including wild-type and mutants, are available. Six structures in their wild-type forms were selected for our study. One was crystallized with the substrate coumarin (1Z10), and the other five were crystallized with inhibitors: methoxsalen (1Z11 [16]), furan analogues (2FDU, 2FDV, 2FDW), and Adrithiol (2FDY [17]), each of which contains 4 chains.

All water molecules were removed, and hydrogen atoms were added using Protein Preparation Wizard in Maestro [22]. Then, the energy-minimization was performed, which optimized the orientation of hydrogen while restraining the conformation of the protein backbones.

2.2. Preparation of NNK and heme

The initial three-dimensional structure of NNK was generated by Ligprep v2.3 [22]. Geometrical optimization and the electrostatic potential calculations were executed at the B3LYP/6-31G** level using the Gaussian03 program [23]. Atomic charges were derived using the restrained electrostatic potential (RESP) fitting procedure [24] in Amber10 [25], which ensured that the derived atom charges were compatible with the standard AMBER force field.

The oxo-ferryl form (compound **I**) of heme was used for the active species (Fig. 1b), which has an oxygen atom (O_{FE}) at the sixth coordination position of iron. The bond length of Fe=O was set to 1.67 Å according to the previous work [26]. All original heme molecules in the crystal structures were displaced by compound **I**. The geometrical optimization of the heme-thiolate complex was performed at the HF/6-31G* level, and atomic charges were derived using the RESP fitting procedure. The force field parameters of compound **I** were adopted from Seifert's work [27].

2.3. Molecular docking

The initial CYP2A–NNK complex models were obtained by molecular docking. Molecular docking was carried out using Glide v5.5 [22], with the standard precision (SP) mode at first followed by the extra precision (XP) mode. The residues within 6 Å of compound **I** were defined as the binding pocket. The output solutions were set to 10 for each chain. The GlideScore was used for ranking the output. The complexes with a low score and oxidation sites (C9 or/and C10) within 4.5 Å of O_{FE} were selected for subsequent MD simulations.

2.4. MD simulations

The starting structures for MD simulation were taken from the above docking results. The protonation state of the residues in each complex was calculated using PROPKA [28]. According to the results for CYP2A13, His84, His164, His229, and His254 were fully protonated at both nitrogen atoms, His328 and His415 were protonated at the ε nitrogen, and all other histidines were protonated at the δ nitrogen. For CYP2A6, His229 and His254 were fully protonated, His328 and His477 were protonated at the ε nitrogen and the rest were protenated at the δ nitrogen. In addition, Glu448 was set to the protonation state (pK_a = 8.17 to 8.27).

All crystal water molecules were kept except for the one that bridged indole and Asn297 in CYP2A13, because this position was already occupied by NNK. The number of this water molecule in the PDB file was Wat1241, 1242, 1243, 1244, 1245, and 1246 for chain A, B, C, D, E, and F, respectively. The all-atom complex models were constructed using Leap in Amber10 and neutralized by adding counterions. The treated models were solvated with water in a truncated octahedron periodic box in which the distance between the box edges and the protein was 10.0 Å. The TIP3P model was used for water.

MD simulations were performed using the Sander module in Amber10. The AMBER ff03 all atom force field [29] was used for the protein, and the general AMBER force field [30] was used for NNK. Energy minimization was conducted in two stages. First, to release the collision from solvents and hydrogen atoms, a 20-ps MD simulation was executed in which only waters, ions, and hydrogen atoms were allowed to move. Next, the minimizations were executed with the backbone atoms restrained by a force constant of 10, 5, and 0 kcal/mol $Å^{-2}$ orderly. In each minimization, 1000

steps with the steepest descent method followed by 2000 steps with the conjugated gradient method were carried out. After minimization, the systems were heated gradually from 0 to 300 K over 60 ps under the NVT ensemble condition and then equilibrated at 300 K for 50 ps. Finally, 6-ns unrestrained MD simulations at 1 atm and 300 K under the NPT ensemble condition were conducted for each system. A time step of 2 fs and a nonbonding interaction cutoff radius of 10.0 Å were used. Coordinates were saved every 1 ps during the entire process.

2.5. Binding free energy calculation

The binding free energy was calculated using the MM-GBSA approach [31], which is based on the following formula:

$$\Delta G = \Delta G_{MM} + \Delta G_{solv} - T\Delta S \quad (1)$$

where ΔG is the free energy of the complex, the protein or the ligand; ΔG_{MM} is the molecular mechanical energy; ΔG_{solv} is the solvation energy; and $T\Delta S$ is the entropy contribution. The molecular mechanical energy is calculated by:

$$\Delta G_{MM} = \Delta G_{int} + \Delta G_{elec} + \Delta G_{vdw} \quad (2)$$

where ΔG_{int} is internal energy and ΔG_{elec}, and ΔG_{vdw} represent the electrostatic and van der Waals (vdW) energy in the gas phase, respectively. The solvation energy is divided into two components:

$$\Delta G_{solv} = \Delta G_{ele,\,sol} + \Delta G_{nonpol,\,sol} \quad (3)$$

where $\Delta G_{ele,sol}$ is the electrostatic contribution to solvation energy and $\Delta G_{nonpol,sol}$ is the nonpolar solvation term. Here, the polar contribution was calculated by solving the modified GB model described by Onufriev et al. [32], whereas the latter is determined using:

$$\Delta G_{nonpol,sol} = \gamma(\mathrm{SASA}) + b \quad (4)$$

where γ represents surface tension and b is constant. They were set to 0.0072 kcal/mol Å^{-2} and 0, respectively, as in the work of Still and co-workers [33]. SASA is the solvent-accessible surface area (Å^2). Finally, the binding free energy of the whole system is calculated by:

$$\Delta G_{bind} = G_{complex} - (G_{protein} + G_{ligand}) \quad (5)$$

In this study, 200 snapshots from the last 2 ns of MD trajectories excluding water and ions were extracted for binding free energy calculations. The polar contribution in terms of solvation energy was calculated using the GBSA program in Amber10. The interior dielectric constant was set to 1.0, and the outer dielectric constant was set to 80.0. The solvent-accessible surface area was determined using the LCPO method [34]. Normal mode analysis [35] was conducted to estimate the entropic changes using the Nmode program in Amber10. The entropy analysis would be computationally expensive and time-wasting if the entire CYP-complex was included in the calculations. To reduce the computational time and decrease the deviation of entropic calculations, an improved method was applied in this study [36]. Only residues and water molecules 12 Å from the ligand were included for normal mode analysis, and the residues located 8–12 Å from the ligand and all water molecules were treated as a buffer region. The same snapshots of each system were extracted for entropy calculations. The truncated structures were minimized for up to 10,000 cycles to give an energy gradient of 0.01 kcal/mol Å^{-1} using a distance-dependent dielectric constant of $\varepsilon = 1.0$.

To obtain the detailed interactions between the protein residues and the substrate, the binding free energy was decomposed onto each individual residue. The MM-GBSA program with the ICOSA method [37] was used for this purpose. Gas-phase energies, desolvation free energies and molecular mechanism were considered in energy decomposition. The parameter settings were similar to the binding free energy analysis.

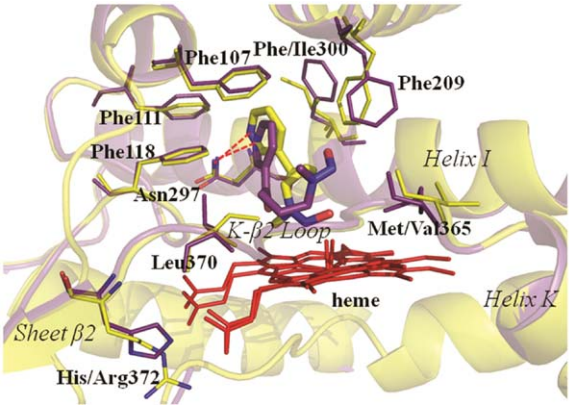

Fig. 2. Superposition of two CYP2A-NNK models from 2P85_E (CYP2A13) and 2FDU_A (CYP2A6), generated by *Glide* XP docking. The residues are labeled by bold font and protein secondary structures are labeled by italic. CYP2A13 is in purple and CYP2A6 in yellow. NNK is shown in thick stick; heme (in red) and residues around the ligand are shown in thin stick. The H-bond is labeled by the red dashed. (For interpretation of the references to color in this figure legend, the reader is referred to the web version of the article.)

3. Results

3.1. CYP2A–NNK complex models obtained by molecular docking

At present, the crystal structures of CYP2A13 and CYP2A6 complexed with NNK are unavailable. Therefore, the CYP2A–NNK complex models were predicted using molecular docking. According to the docking outputs, the binding poses were divided into two cases. Case 1: either the pyridine portion of NNK oriented to the heme or both C9 and C10 were greater than 4.5 Å from O_{FE}. The orientations of NNK in this case were assumed to be undesirable, because they are not beneficial for the catalytic oxidation. Case 2: the head portion of NNK oriented to the heme, and either C9 or C10 was within 4.5 Å from O_{FE}. The orientation of NNK in this case was considered to be desirable. The statistical results from the docking scores are shown in Table 1.

As seen in Table 1, the docking scores cannot obviously discriminate a preference between CYP2A13 and CYP2A6 bound with NNK. For example, the average scores of NNK with CYP2A6 (2FDU) were very close to those of CYP2A13, with no obvious difference in binding modes between them (Supporting information, Fig. S1). In addition, there were remarkable differences between the CYP2A6 structures, which implies that protein flexibility has a significant effect on substrate binding. Because Glide was a rigid docking process and the flexibility of the receptor was not considered, MD simulations were adopted to refine the NNK–CYP2A complexes.

To obtain the reliable starting structure for MD simulations, NNK was docked into CYP2A13 and CYP2A6 (2FDU) again using Glide with XP mode. One solution was outputted for each chain. The results are listed in Table 1. All poses belonged to the desirable pose except 2P85_D, which did not meet our requirements. Previous studies reported that Asn297 was a key residue and acted as an H-bond donor, which not only guided an optimal ligand orientation, but also stabilized the substrate binding in the active site [38–40]. This suggested that the formation of the H-bond was important to substrate metabolism. Thus 2P85_A and C and 2FDU_B were excluded. Among the remaining six complexes, 2P85_E and 2FDU_A (see Fig. 2), which had the lowest XP docking scores, were selected as the starting structures for MD simulations. To validate the result, 2P85_B and 2FDU_C were also chosen to perform the MD

Table 1
Statistical results of docking scores and pose classifications.

PDB code (resolution)	Chain	Standard precision				Extra precision		
		Lowest score	Average score	Case 2		Distance (Å)[a]	H-bond acceptor	Score
				Number	Ave. score			
CYP2A13								
2P85 (2.35 Å)	A	−5.925	−5.397	10	−5.397	4.412 (C10)	–	−7.294
	B	−6.233	−5.667	10	−5.667	2.977 (C9)	N1	−7.773
	C	−6.578	−6.385	9	−6.469	3.441 (C9)	–	−8.096
	D	−6.102	−5.824	10	−5.824	5.209 (C9)	O1	−8.377
	E	−6.003	−5.433	10	−5.433	3.194 (C9)	N1	−7.936
	F	−5.897	−5.533	8	−5.543	2.779 (C10)	N1	−7.419
CYP2A6								
2FDU (1.85 Å)	A	−5.639	−4.973	9	−5.021	3.154 (C10)	N1	−7.603
	B	−6.002	−5.333	9	−5.413	3.589 (C10)	–	−7.674
	C	−5.695	−4.901	10	−4.901	2.977 (C9)	N1	−6.575
	D	−6.277	−5.191	7	−5.504	2.890 (C10)	N1	−6.554
2FDV (1.65 Å)	A	−5.434	−4.998	10	−4.998			
	B	−6.147	−4.962	8	−5.077			
	C	−5.932	−4.858	8	−4.943			
	D	−5.869	−4.999	7	−5.248			
2FDW (2.05 Å)	A	−5.403	−4.891	8	−4.959			
	B	−5.325	−4.501	9	−4.589			
	C	−5.561	−4.616	7	−4.817			
	D	−5.404	−4.508	8	−4.628			
2FDY 1.95 Å)	A	−6.114	−5.350	10	−5.350			
	B	−5.991	−5.291	9	−5.413			
	C	−5.955	−5.064	9	−5.065			
	D	−6.196	−5.313	8	−5.501			
1Z10 1.90 Å)	A	−5.418	−4.864	8	−5.019			
	B	−3.959	−3.959	1	−3.959			
	C	−4.169	−3.817	4	−3.909			
	D	−4.306	−4.146	0	/			
1Z11 2.05 Å)	A	−5.645	−4.356	8	−4.268			
	B	−4.288	−4.532	4	−4.755			
	C	−5.017	−4.166	8	−4.126			
	D	−5.100	−4.665	4	−4.582			

[a] The distance between atom O_{FE} of heme and atom C9 or C10 of NNK.

simulations in the same procedure, and some of those results are presented in the Supporting information.

3.2. MD simulations

MD simulations were carried out on each complex under the same condition. To assess the stability of the complexes, the RMSD value relative to the initial structure was monitored. Fig. 3 shows the RMSD values of two complex systems during a 6-ns MD simulations. The RMSD of backbone atoms and protein atoms maintained ~1.2 Å and ~2 Å, respectively, which indicates that the whole proteins did not significantly deviate from their starting structures after equilibrium. To analyze the conformational changes of local sites and the possible difference in ligand binding modes between the two systems, the average structure from the last 2 ns of each trajectory was calculated, followed by a 2000-step energy-minimization.

3.2.1. H-bond between NNK and Asn297

The average structure was superimposed on the initial structure to check for conformational changes. As shown in Fig. 4a, the orientation of NNK in CYP2A13 did not change significantly after MD refinement, and the N1 atom maintained the hydrogen bond with Asn297. The head portion of NNK showed a slight shift in which the methyl (C10) group approached the heme, and the whole linker moved away somewhat from the helix I. This change caused several residues in the K-β2 loop, especially Met365 and Leu366, to move outwards so as to allow more space for NNK binding. In contrast, NNK underwent a remarkable change after MD simulations with CYP2A6, as shown in Fig. 4b. The pyridine portion moved to the upper edge of the binding pocket, and the H-bond acceptor changed to the O1 atom of the carbonyl group instead of N1. Correspondingly, the residues at the K-β2 loop did not obviously change, but the side chains of the Phe-cluster, such as Phe107 and Phe209, altered their conformations to adapt to the adjustment of NNK.

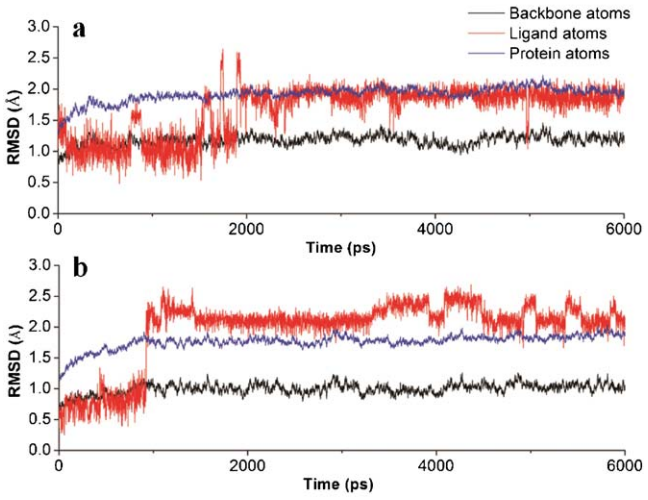

Fig. 3. The RMSD value related time of complexes in MD simulation. (a) CYP2A13 complex; (b) CYP2A6 complex.

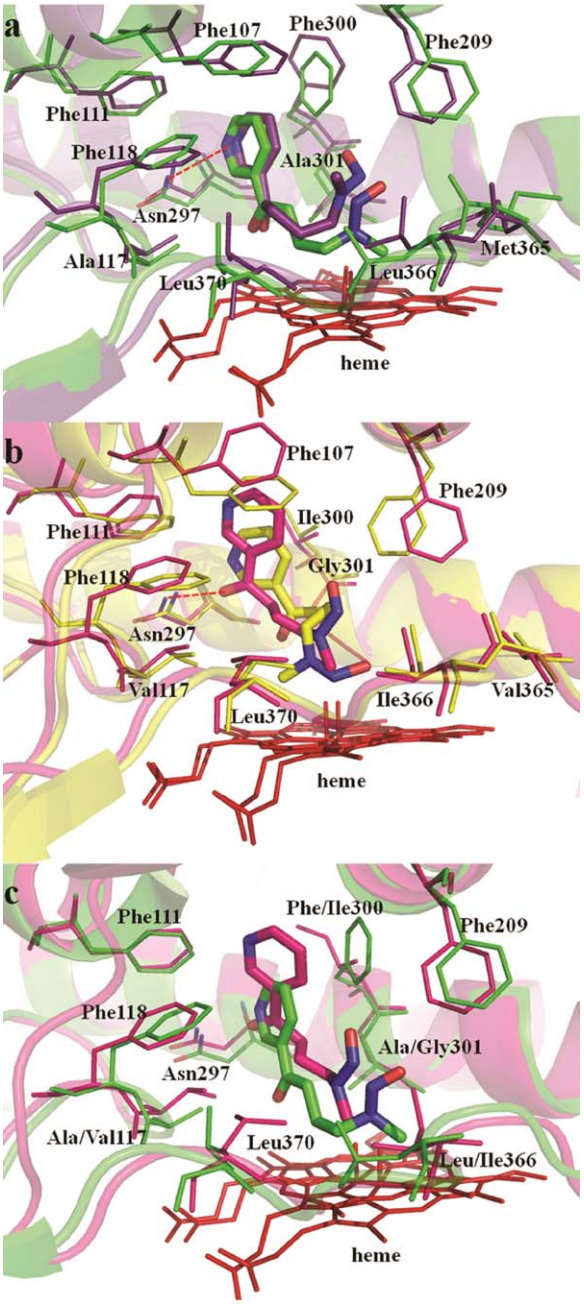

Fig. 4. Average structures from last 2 ns in MD trajectory superimposed on starting structure of (a) CYP2A13 complex and (b) CYP2A6 complex; (c) average structure superposition of CYP2A13 and CYP2A6. The starting structure is in purple for CYP2A13 and in yellow for CYP2A6; the average structure from MD simulation is in green for CYP2A13 and in magenta for CYP2A6. NNK is shown in thick stick; heme (in red) and residues around the ligand are shown in thin stick. The H-bond is labeled by the red dashed.

3.2.2. Hydrophobic residues in the binding site

A series of hydrophobic residues in both CYP2A13 and CYP2A6 played important roles in CYP2A–NNK interactions. Among the Phe-cluster, Phe107, Phe111, and Phe209 constituted the hydrophobic edge of the binding pocket and contacted with NNK through vdW interactions, and Phe118 formed a face-to-edge (T-shaped) π–π interaction with the pyridine ring (Fig. 4).

Structural superposition of CYP2A13 and CYP2A6 displayed several different hydrophobic residues that influenced NNK binding, as shown in Fig. 4c. Ala301 in CYP2A13 oriented its methyl group to the binding site, which pushed NNK away from helix I. In contrast, Gly301 in the same position on CYP2A6 had no such steric hindrance, thus NNK was closer to helix I. In addition, the side chains of either Ala117 or Val117 pointed to the binding site. Compared to alanine, valine is a larger residue, which occupied part of the space for the NNK linker, thereby making NNK approach helix I. The relatively small size of Ala117 left more space and allowed the ligand to shift toward it. These two non-identical residues at position 301 and 117 are located on the opposite sides of the binding site, which resulted in different shapes and volumes for the binding sites in CYP2A6 and CYP2A13. This could explain why the H-bond acceptor changed between the two proteins. There would be a collision with Ala301 if NNK moved up.

The residue at position 300 was another important residue that contacted with the ligand. Ile300 in CYP2A6 pointed its side chain to NNK and thus had a strong vdW interaction with it. On the other hand, Phe300 in CYP2A13 was not as close to NNK as Ile300 (3.5–4 Å from NNK). However, Phe300 intermittently formed parallel-displaced π–π interactions with the pyridine ring of NNK [41,42] during MD simulations.

3.3. Binding free energy analysis

3.3.1. Binding free energy and its components

To gain insights into the difference in the binding affinity for NNK with the two isozymes, the binding free energies were calculated using the MM-GBSA method. Table 2 lists the calculation results, including the total energy and its individual components. The binding free energy of NNK with CYP2A13 is lower than that of CYP2A6. The ΔG^{cal}_{bind} difference between CYP2A13 and CYP2A6 was ~2.03 kcal/mol, which suggested NNK was more stable in CYP2A13.

3.3.2. Binding free energy decomposition

To obtain the detailed interactions between NNK and the enzymes, the binding free energies were decomposed on each residue using the MM-GBSA approach. The residues involved in the protein–ligand interactions are listed in Table 3.

As expected, Asn297 contributed the most to NNK binding in both systems, because a strong H-bond was formed between Asn297 and the substrate. However, the two other residues at positions 300 and 301 in helix I differed in the contribution to the NNK binding between CYP2A13 and CYP2A6. Phe300/Ile300 was the major vdW contributor. Ala301 contributed more than Gly301, because its methyl group contacted with NNK. In CYP2A13, these interactions were strengthened by Leu366 and Leu370 on the K-β2 loop. Helix I and the K-β2 loop on the opposite side of the ligand acted as a clamp to stabilize the NNK in CYP2A13, whereas NNK in CYP2A6 was closer to the Phe-cluster and thus preferred to interact with these phenylalanines. This was the main difference in the vdW interactions between the two systems.

4. Discussion

Because the CYP2A–NNK crystal structures are not available at present, we first constructed models of the CYP2A–NNK complex. Docking has become a commonly used tool to reveal the interactions between ligands and receptors, but docking results are sensitive and often affected by slight conformational changes of residues [43]. Additionally, docking scores are not reliable enough to differentiate between similar binding modes [44]. In this study, the docking scores of the individual structures did not discriminate the binding preference between CYP2A13 and CYP2A6 with NNK. For example, 2FDU had the best score results among the CYP2A6 structures, and its poses were similar to those of 2P85 (CYP2A13). Furthermore, the chains within the same structure had slightly different scores, which suggested that small changes in the active site

Table 2
Binding free energy of CYPs with NNK in kcal/mol calculated by MM-GBSA method.

CYP[a]		ΔG_{elec}[b] (± ste)[c]	ΔG_{vdw}[b] (± ste)[c]	$\Delta G_{ele,sol}$[b] (± ste)[c]	$\Delta G_{nonp,sol}$[b] (± ste)[c]	$T\Delta S$[b] (± ste)[c]	ΔG_{bind}^{cal}	ΔG_{bind}^{exp}[d]
2A13	Com.	−12340.06 (11.99)	−2278.27 (2.34)	−5735.87 (10.55)	147.23 (0.09)	589.99 (0.32)		
	Rec.	−12196.33 (11.98)	−2252.11 (2.32)	−5739.60 (10.52)	148.42 (0.09)	579.80 (0.33)		
	Lig.	−130.15 (0.09)	9.10 (0.11)	−23.47 (0.07)	3.04 (0.01)	38.12 (0.37)		
	Delta	−13.58 (0.17)	−35.25 (0.13)	27.20 (0.12)	−4.23 (0.01)	−18.93 (0.37)	−6.93	−7.34 [11]
2A6	Com.	−12785.94 (6.62)	−2290.20 (2.30)	−5388.40 (5.74)	146.72 (0.08)	614.18 (0.35)		
	Rec.	−12641.31 (6.56)	−2265.41 (2.31)	−5393.95 (5.73)	147.83 (0.08)	595.76 (0.31)		
	Lig.	−131.61 (0.09)	9.23 (0.13)	−21.92 (0.06)	2.99 (0.01)	37.19 (0.33)		
	Delta	−13.02 (0.16)	−34.02 (0.13)	27.47 (0.13)	−4.10 (0.01)	−18.77 (0.36)	−4.90	−5.40 [7]

[a] *Abbreviations*: Com. = complex, Rec. = receptor and Lig. = ligand.
[b] Average calculated with 200 snapshots from 4 to 6 ns trajectory.
[c] Standard error of the mean.
[d] Calculated from the experimental data K_m via $\Delta G_{bind}^{exp} \approx RT \ln K_m$ at $T = 300$ K.

residues could lead to diversity in the results. For these reasons, the interactions of NNK with CYP2A enzymes were re-evaluated using further MD simulations.

MD simulation fully considers the flexibility of proteins, which allows the protein to adapt to the adjustment of the ligand in its binding pocket. In this study, an obvious change after MD refinement was observed for the H-bond acceptor of NNK when complexed with CYP2A6. Previous studies have shown that Asn297 always formed the H-bond with ligands in CYP2A and significantly affected the binding of NNK [15–17,19]. The H-bond formation was considered to be a prerequisite for the selection of a starting structure in our earlier molecular docking. We monitored the H-bonds between Asn297 and the ligand during MD simulations. The results of heavy atoms involved in H-bonding and the occupancy are listed in Table 4. These results indicate that Asn297 acts as the H-bond donor in both systems. Asn297 showed hydrogen bonding with the N1 atom in CYP2A13, but bonded with the O1 atom in CYP2A6. However, this did not affect the orientation of the NNK head portion in either system and still enabled the possible oxidation site of NNK to point to the heme, which is evidenced by the measured distances between the two sites of metabolism of NNK and the O atom of compound **I** (Supporting information, Fig. S2). All the distances are within 4.5 Å.

As shown in Fig. 4, NNK contacted more with the residues of helix I in CYP2A13 and kept in a stable state between helix I and the K-β2 loop. In contrast, NNK appeared to mainly interact with helix I and the Phe-cluster in CYP2A6. The binding mode of NNK in the two isozymes showed a high degree of similarity. NNK formed the H-bond interaction with Asn297 and was stabilized by the vdW interactions with the hydrophobic residues in each system. Nevertheless, the dissimilarity may be crucial for the differential binding of NNK in these two systems. The non-identical residues, especially those at positions 117, 300, and 301, led to the different binding modes of NNK in CYP2A13 and CYP2A6. Previous mutation experiments indicated the catalytic activity of CYP2A13 was decreased when these residues were substituted into the corresponding position in CYP2A6 [20]. Our results showed that the influence of these residues toward NNK was complementary. First, residues of different sizes at positions 301 and 117 altered the shape of the binding site. To fit the individual binding pocket, NNK adjusted its binding orientation, and this resulted in the change of the H-bond acceptor. Next, either Phe300 or Ile300 directly contacted NNK and played

Table 3
Residue energy contributions of CYPs for NNK binding in kcal/mol.[a]

Res. No.	CYP2A13		CYP2A6	
	Residue	$\Delta G_{bind}^{res} \pm$ ste	Residue	$\Delta G_{bind}^{res} \pm$ ste
107	Phe	−0.82 ± 0.02	Phe	−1.34 ± 0.03
111	Phe	−0.41 ± 0.01	Phe	−0.47 ± 0.02
117	Ala	−0.66 ± 0.01	Val	−0.79 ± 0.03
118	Phe	−1.11 ± 0.02	Phe	−1.04 ± 0.02
208	Ser	−0.04 ± 0.01	Ile	−0.42 ± 0.01
209	Phe	−0.68 ± 0.02	Phe	−0.62 ± 0.01
297	Asn	−2.31 ± 0.04	Asn	−2.28 ± 0.04
300	Phe	−1.98 ± 0.03	Ile	−1.76 ± 0.02
301	Ala	−1.42 ± 0.03	Gly	−0.86 ± 0.01
305	Thr	−0.68 ± 0.02	Thr	−0.39 ± 0.02
365	Met	−0.58 ± 0.02	Val	−0.02 ± 0.01
366	Leu	−0.96 ± 0.02	Ile	−0.67 ± 0.02
370	Leu	−0.91 ± 0.01	Leu	−0.81 ± 0.03
480	Phe	−0.01 ± 0.01	Phe	−0.74 ± 0.02
Ligand	NNK	−11.42 ± 0.07	NNK	−10.66 ± 0.08

[a] The residues with $\Delta G_{bind}^{res} < -0.50$ kcal/mol of each system are shown, and for comparison, those residues in the corresponding position of the other system were also presented.

Table 4
Hydrogen bonds corresponding to NNK binding in both CYPs.

CYP	H-bond donor[a]			H-bond acceptor		Distance (Å)[b]	Occupancy (%)[c]
2A13	Asn297	ND2	HD22	NNK	N1	3.118	89.95
	Wat975	O	H1	Heme	O1A	2.759	99.10
					O2A	3.196	42.50
			H2	His372	NE2	2.932	92.35
2A6	Asn297	ND2	ND22	NNK	O1	3.001	93.30
	Arg372	NE	HE	Heme	O2A	3.164	82.00
					O1A	3.239	79.35
	Wat2510	O	H1	Heme	O1A	2.793	98.15
					O2A	3.014	77.55
			H2	Leu340	O	2.812	98.05

[a] The identifier of water molecule is consistent with it in original PDB file.
[b] Average distance between acceptor atom and donor atom during 4–6 ns simulation.
[c] Occupancy is hydrogen bond present percentage during 4–6 ns simulation.

an important role in the vdW interaction. Previous studies have demonstrated that F300I substitution in CYP2A13 leads to a significant decrease in V_{max}/K_m toward other substrates [19,20]. This was thought to be due to the fact that, compared to Ile300 in CYP2A6, the side chain of Phe300 in CYP2A13 rotated out from the active site slightly and thus left more space for ligand binding. Our MD simulations showed that Phe300 also provides an extra π–π interaction with NNK. The parallel-displaced π–π interaction between benzene and pyridine is considered to be a kind of stable form in protein stability [45,46]. Taken together, the collective roles of Asn297, Phe300, Ala301 and Ala117 made the shape of the active site more favorable for NNK binding in CYP2A13.

Residues in the K-β2 loop were also located in the binding site, but they are not conserved across these two isozymes. Four of ten residues differ. Among them, the residue at position 372 was reported to be a key residue for ligand binding. The H372R mutation in CYP2A13 led to a 20-fold increase in the K_m and a 7-fold decrease in the V_{max} for the oxidation of NNK [21]. Fig. 5 shows the K-β2 loops of the two CYP2A enzymes superimposed. Arg372 formed a direct H-bond with the 7-propionate of the heme in CYP2A6, whereas His372 in CYP2A13 interacted with the heme via an ordered water bridge (Wat975) (Table 4). For this reason, the K-β2 loop in CYP2A6 was closer to the heme than in CYP2A13, so that the binding pocket of CYP2A6 shrank somewhat. Additionally, this residue in other CYPs has been reported to act as a water channel switch and stabilize the heme by salt bridging [47,48]. The water channel has been suggested to be a factor in catalytic activity [47,49]. Based on this, His/Arg372 acting as the channel switch might affect the binding and catalysis via the hydration. In addition, an ordered water molecule (Wat2510) bridged the backbone oxygen of Leu370 and the heme in CYP2A6 (Table 4), whereas Leu370 in CYP2A13 was too distant to interact with the heme. The residues in the K-β2 loop, such as Leu370, contacted with the ligand and played important roles in complex stabilization [19]. It is possible that the flexibility of the K-β2 loop in CYP2A13 allowed its residues more freedom and thus left more space for ligand binding, which facilitated the binding of NNK to the active site. To support this idea, we have calculated the active site volumes of both systems using SiteMap v2.3 [22]. The calculated active site volume of CYP2A13 is 169 $Å^3$, which is larger than 149 $Å^3$ of CYP2A6.

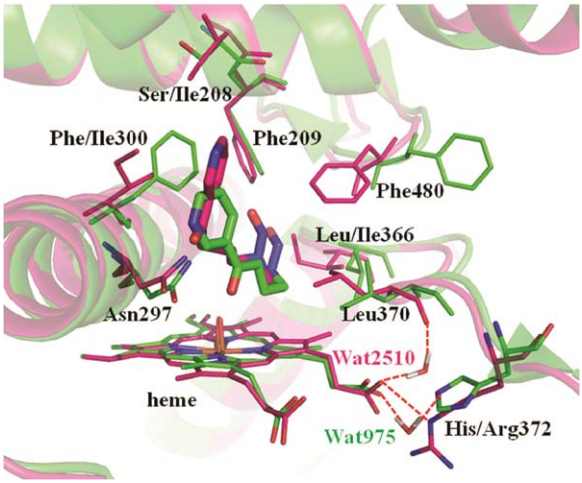

Fig. 5. Average structure superposition of CYP2A13 complex and CYP2A6 complex. The color scheme is the same as Fig. 4. Heme was shown in atom type. The H-bond is labeled by the red dashed. (For interpretation of the references to color in this figure legend, the reader is referred to the web version of the article.)

MM-GBSA is commonly used to estimate the free energy and has been included in previous studies [50,51]. In this study, the calculated binding free energy of NNK with CYP2A13 was lower than that of CYP2A6 by about 2.03 kcal/mol, which is in line with the previous biochemical data (Table 2). According to previous studies, the K_m of the NNK oxidation by CYP2A13 was ~20-60 times lower and the V_{max}/K_m ~300 times higher than by CYP2A6 [52]. Generally, the smaller the apparent K_m of the substrate is, the greater the affinity of the substrate on an enzyme is [53]. Differences in each individual energy component were not obvious between the two enzymes, which suggested that the nature of NNK binding was similar in both CYPs. Among these components, the vdW energy makes the largest contribution, which is consistent with the fact that the active sites of CYP2A13 and CYP2A6 are primarily composed of hydrophobic residues. The difference between the vdW terms is also the most obvious. This was mainly attributed to the different conformations of the non-identical residues in the active sites of the two enzymes. The volume and shape of the binding site in CYP2A13 was more suitable for NNK binding.

Residue 208 has been reported to affect NNK oxidation. The S208I mutation in CYP2A13 led to a 10-fold decrease in the V_{max}/K_m [21]. In this study, it appeared that neither Ser208 nor Ile208 influenced NNK binding directly, though Ile208 had some hydrophobic contribution. Previous studies on other CYPs have indicated that there is a solvent channel lined by helix-E, -F, and -I, which controlled proton access to the active site [54,55]. Thus, it is possible that residue 208 plays a role in the access/exit of NNK to the active site.

5. Conclusions

Molecular docking combined with MD simulations and free energy calculations was performed on CYP2A13 and CYP2A6 in complex with NNK, which aimed to reveal the structural determinants accounting for the differential catalytic activity of the two

isozymes toward NNK. Our results demonstrated that NNK formed a hydrogen bond with the same donor, Asn297, but the acceptors differed. In CYP2A13, the binding of NNK was affected by Ala301, Phe300, and Ala117, and the N1 atom maintained the H-bond with Asn297. In CYP2A6, the H-bond acceptor changed to the O1 atom and NNK preferred to interact with the Phe-cluster. The vdW interaction was the major contributor to NNK binding and also showed the most obvious differences between two systems. These differences led to the change in H-bond acceptors. In addition, the K-β2 loop contacted closely with NNK and was flexible enough to adapt to NNK binding in CYP2A13, whereas a similar effect of the K-β2 loop in CYP2A6 was not so obvious. Binding free energy analysis indicated that NNK had a lower binding energy with CYP2A13, which is consistent with the biochemical experimental data. These findings clarified the structural role of the residues within the active site of CYP2A13 and CYP2A6 in the difference in catalytic activity toward NNK and could be helpful in understanding the functional roles of CYP2A in the catalysis of other substrates.

Acknowledgments

W. Li thanks the financial support from Shanghai Natural Science Foundation (Grant No. 10ZR1407000) and Fundamental Research Funds for the Central Universities (WY1014010). Y. Tang thanks the Program for New Century Excellent Talents in University (Grant No. NCET-08-0774) and the National S&T Major Project of China (Grant No. 2009ZX09501-001). Usage of AMBER is gratefully acknowledged. This work was also supported by Shanghai Supercomputer Center of China.

Appendix A. Supplementary data

Supplementary data associated with this article can be found, in the online version, at doi:10.1016/j.jmgm.2011.05.002.

References

[1] S. Yamano, J. Tatsuno, F.J. Gonzalez, The CYP2A3 gene product catalyzes coumarin 7-hydroxylation in human liver microsomes, Biochemistry 29 (1990) 1322–1329.
[2] S. Koskela, J. Hakkola, J. Hukkanen, O. Pelkonen, M. Sorri, A. Saranen, S. Anttila, P. Fernandez-Salguero, F. Gonzalez, H. Raunio, Expression of CYP2A genes in human liver and extrahepatic tissues, Biochem. Pharmacol. 57 (1999) 1407–1413.
[3] J. Gu, T. Su, Y. Chen, Q.Y. Zhang, X. Ding, Expression of biotransformation enzymes in human fetal olfactory mucosa: potential roles in developmental toxicity, Toxicol. Appl. Pharmacol. 165 (2000) 158–162.
[4] S.S. Hecht, Biochemistry, biology, and carcinogenicity of tobacco-specific N-nitrosamines, Chem. Res. Toxicol. 11 (1998) 559–603.
[5] S.G. Carmella, M. Ye, P. Upadhyaya, S.S. Hecht, Stereochemistry of metabolites of a tobacco-specific lung carcinogen in smokers' urine, Cancer Res. 59 (1999) 3602–3605.
[6] S.S. Hecht, Tobacco smoke carcinogens and lung cancer, J. Natl. Cancer Inst. 91 (1999) 1194–1210.
[7] C.J. Patten, T.J. Smith, S.E. Murphy, M.H. Wang, J. Lee, R.E. Tynes, P. Koch, C.S. Yang, Kinetic analysis of the activation of 4-(methylnitrosamino)-1-(3-pyridyl)-1-butanone by heterologously expressed human P450 enzymes and the effect of P450-specific chemical inhibitors on this activation in human liver microsomes, Arch. Biochem. Biophys. 333 (1996) 127–138.
[8] E.S. Messina, R.F. Tyndale, E.M. Sellers, A major role for CYP2A6 in nicotine C-oxidation by human liver microsomes, J. Pharmacol. Exp. Ther. 282 (1997) 1608–1614.
[9] T. Su, Z. Bao, Q.Y. Zhang, T.J. Smith, J.Y. Hong, X. Ding, Human cytochrome P450 CYP2A13: predominant expression in the respiratory tract and its high efficiency metabolic activation of a tobacco-specific carcinogen, 4-(methylnitrosamino)-1-(3-pyridyl)-1-butanone, Cancer Res. 60 (2000) 5074–5079.
[10] J.R. Jalas, X. Ding, S.E. Murphy, Comparative metabolism of the tobacco-specific nitrosamines 4-(methylnitrosamino)-1-(3-pyridyl)-1-butanone and 4-(methylnitrosamino)-1-(3-pyridyl)-1-butanol by rat cytochrome P450 2A3 and human cytochrome P450 2A13, Drug Metab. Dispos. 31 (2003) 1199–1202.
[11] X. Zhang, T. Su, Q.Y. Zhang, J. Gu, M. Caggana, H. Li, X. Ding, Genetic polymorphisms of the human CYP2A13 gene: identification of single-nucleotide polymorphisms and functional characterization of an Arg257Cys variant, J. Pharmacol. Exp. Ther. 302 (2002) 416–423.
[12] T. Fukami, M. Katoh, H. Yamazaki, T. Yokoi, M. Nakajima, Human cytochrome P450 2A13 efficiently metabolizes chemicals in air pollutants: naphthalene, styrene, and toluene, Chem. Res. Toxicol. 21 (2008) 720–725.
[13] T. Fukami, M. Nakajima, H. Sakai, M. Katoh, T. Yokoi, CYP2A13 metabolizes the substrates of human CYP1A2, phenacetin, and theophylline, Drug Metab. Dispos. 35 (2007) 335–339.
[14] X.Y. He, L. Tang, S.L. Wang, Q.S. Cai, J.S. Wang, J.Y. Hong, Efficient activation of aflatoxin B1 by cytochrome P450 2A13, an enzyme predominantly expressed in human respiratory tract, Int. J. Cancer 118 (2006) 2665–2671.
[15] B.D. Smith, J.L. Sanders, P.R. Porubsky, G.H. Lushington, C.D. Stout, E.E. Scott, Structure of the human lung cytochrome P450 2A13, J. Biol. Chem. 282 (2007) 17306–17313.
[16] J.K. Yano, M.H. Hsu, K.J. Griffin, C.D. Stout, E.F. Johnson, Structures of human microsomal cytochrome P450 2A6 complexed with coumarin and methoxsalen, Nat. Struct. Mol. Biol. 12 (2005) 822–823.
[17] J.K. Yano, T.T. Denton, M.A. Cerny, X. Zhang, E.F. Johnson, J.R. Cashman, Synthetic inhibitors of cytochrome P-450 2A6: inhibitory activity, difference spectra, mechanism of inhibition, and protein cocrystallization, J. Med. Chem. 49 (2006) 6987–7001.
[18] X.Y. He, J. Shen, W.Y. Hu, X. Ding, A.Y. Lu, J.Y. Hong, Identification of Val117 and Arg372 as critical amino acid residues for the activity difference between human CYP2A6 and CYP2A13 in coumarin 7-hydroxylation, Arch. Biochem. Biophys. 427 (2004) 143–153.
[19] N.M. DeVore, B.D. Smith, M.J. Urban, E.E. Scott, Key residues controlling phenacetin metabolism by human cytochrome P450 2A enzymes, Drug Metab. Dispos. 36 (2008) 2582–2590.
[20] N.M. DeVore, B.D. Smith, J.L. Wang, G.H. Lushington, E.E. Scott, Key residues controlling binding of diverse ligands to human cytochrome P450 2A enzymes, Drug Metab. Dispos. 37 (2009) 1319–1327.
[21] X.Y. He, J. Shen, X. Ding, A.Y. Lu, J.Y. Hong, Identification of critical amino acid residues of human CYP2A13 for the metabolic activation of 4-(methylnitrosamino)-1-(3-pyridyl)-1-butanone, a tobacco-specific carcinogen, Drug Metab. Dispos. 32 (2004) 1516–1521.
[22] Maestro v9.0, Ligprep v2.3, Protein Preparation Wizard, Glide v5.5: Schrödinger, LLC, New York, NY.
[23] M.J. Frisch, G.W. Trucks, H.B. Schlegel, G.E. Scuseria, M.A. Robb, J.R. Cheeseman, J.A. Montgomery, T. Vreven Jr., K.N. Kudin, J.C. Burant, J.M. Millam, S.S. Iyengar, J. Tomasi, V. Barone, B. Mennucci, M. Cossi, G. Scalmani, N. Rega, G.A. Petersson, H. Nakatsuji, M. Hada, M. Ehara, K. Toyota, R. Fukuda, J. Hasegawa, M. Ishida, T. Nakajima, Y. Honda, O. Kitao, H. Nakai, M. Klene, X. Li, J.E. Knox, H.P. Hratchian, J.B. Cross, C. Adamo, J. Jaramillo, R. Gomperts, R.E. Stratmann, O. Yazyev, A.J. Austin, R. Cammi, C. Pomelli, J.W. Ochterski, P.Y. Ayala, K. Morokuma, G.A. Voth, P. Salvador, J.J. Dannenberg, V.G. Zakrzewski, S. Dapprich, A.D. Daniels, M.C. Strain, O. Farkas, D.K. Malick, A.D. Rabuck, K. Raghavachari, J.B. Foresman, J.V. Ortiz, Q. Cui, A.G. Baboul, S. Clifford, J. Cioslowski, B.B. Stefanov, G. Liu, A. Liashenko, P. Piskorz, I. Komaromi, R.L. Martin, D.J. Fox, T. Keith, M.A. Al-Laham, C.Y. Peng, A. Nanayakkara, M. Challacombe, P.M.W. Gill, B. Johnson, W. Chen, M.W. Wong, C. Gonzalez, J.A. Pople, Gaussian 03. Gaussian, Inc., Pittsburgh, PA, 2003.
[24] M.K. Gilson, K.A. Sharp, B.H. Honig, Calculating the electrostatic potential of molecules in solution, J. Comput. Chem. 9 (1988) 327.
[25] D.A. Case, T.A. Darden, T.E. Cheatham III, C.L. Simmerling, J. Wang, R.E. Duke, R. Luo, M. Crowley, R.C. Walker, W. Zhang, K.M. Merz, B. Wang, S. Hayik, A. Roitberg, G. Seabra, I. Kolossváry, K.F. Wong, F. Paesani, J. Vanicek, X. Wu, S.R. Brozell, T. Steinbrecher, H. Gohlke, L. Yang, C. Tan, J. Mongan, V. Hornak, G. Cui, D.H. Mathews, M.G. Seetin, C. Sagui, V. Babin, P.A. Kollman, AMBER 10, University of California, San Francisco, 2008.
[26] I. Schlichting, J. Berendzen, K. Chu, A.M. Stock, S.A. Maves, D.E. Benson, R.M. Sweet, D. Ringe, G.A. Petsko, S.G. Sligar, The catalytic pathway of cytochrome p450cam at atomic resolution, Science 287 (2000) 1615–1622.
[27] A. Seifert, S. Tatzel, R.D. Schmid, J. Pleiss, Multiple molecular dynamics simulations of human p450 monooxygenase CYP2C9: the molecular basis of substrate binding and regioselectivity toward warfarin, Proteins 64 (2006) 147–155.
[28] H. Li, A.D. Robertson, J.H. Jensen, Very fast empirical prediction and rationalization of protein pK_a values, Proteins 61 (2005) 704–721.
[29] Y. Duan, C. Wu, S. Chowdhury, M.C. Lee, G. Xiong, W. Zhang, R. Yang, P. Cieplak, R. Luo, T. Lee, J. Caldwell, J. Wang, P. Kollman, A point-charge force field for molecular mechanics simulations of proteins based on condensed-phase quantum mechanical calculations, J. Comput. Chem. 24 (2003) 1999–2012.
[30] J. Wang, R.M. Wolf, J.W. Caldwell, P.A. Kollman, D.A. Case, Development and testing of a general amber force field, J. Comput. Chem. 25 (2004) 1157–1174.
[31] P.A. Kollman, I. Massova, C. Reyes, B. Kuhn, S. Huo, L. Chong, M. Lee, T. Lee, Y. Duan, W. Wang, O. Donini, P. Cieplak, J. Srinivasan, D.A. Case, T.E. Cheatham 3rd, Calculating structures and free energies of complex molecules: combining molecular mechanics and continuum models, Acc. Chem. Res. 33 (2000) 889–897.
[32] A. Onufriev, D. Bashford, D.A. Case, Modification of the generalized born model suitable for macromolecules, J. Phys. Chem. B 104 (2000) 3712–3720.
[33] W. Clark Still, Anna Tempczyk, C. Ronald, T. Hawley, Hendrickson, Semianalytical treatment of solvation for molecular mechanics and dynamics, J. Am. Chem. Soc. 112 (1990) 6127–6129.
[34] J. Weiser, P.S. Shenkin, W.C. Still, Approximate atomic surfaces from linear combinations of pairwise overlaps (LCPO), J. Comput. Chem. 20 (1999) 217–230.

[35] B.R. Brooks, D. Janežič, M. Karplus, Harmonic analysis of large systems, I. Methodol. J. Comput. Chem. 16 (1995) 1522–1542.
[36] J. Kongsted, U. Ryde, An improved method to predict the entropy term with the MM/PBSA approach, J. Comput. Aided Mol. Des. 23 (2009) 63–71.
[37] H. Gohlke, C. Kiel, D.A. Case, Insights into protein–protein binding by binding free energy calculation and free energy decomposition for the Ras-Raf and Ras-RalGDS complexes, J. Mol. Biol. 330 (2003) 891–913.
[38] D. Kim, Z.L. Wu, F.P. Guengerich, Analysis of coumarin 7-hydroxylation activity of cytochrome P450 2A6 using random mutagenesis, J. Biol. Chem. 280 (2005) 40319–40327.
[39] W. Li, H. Ode, T. Hoshino, H. Liu, Y. Tang, H. Jiang, Reduced catalytic activity of P450 2A6 mutants with coumarin: a computational investigation, J. Chem. Theory Comput. 5 (2009) 1411–1420.
[40] K.E. Schlicht, J.Z. Berg, S.E. Murphy, Effect of CYP2A13 active site mutation N297A on metabolism of coumarin and tobacco-specific nitrosamines, Drug Metab. Dispos. 37 (2009) 665–671.
[41] G.B. McGaughey, M. Gagne, A.K. Rappe, pi-Stacking interactions. Alive and well in proteins, J. Biol. Chem. 273 (1998) 15458–15463.
[42] M.O. Sinnokrot, E.F. Valeev, C.D. Sherrill, Estimates of the ab initio limit for pi–pi interactions: the benzene dimer, J. Am. Chem. Soc. 124 (2002) 10887–10893.
[43] J. Hritz, A. de Ruiter, C. Oostenbrink, Impact of plasticity and flexibility on docking results for cytochrome P450 2D6: a combined approach of molecular dynamics and ligand docking, J. Med. Chem. 51 (2008) 7469–7477.
[44] M.M. Ahlstrom, M. Ridderstrom, I. Zamora, CYP2C9 structure–metabolism relationships: substrates, inhibitors, and metabolites, J. Med. Chem. 50 (2007) 5382–5391.
[45] E.G. Hohenstein, C.D. Sherrill, Effects of heteroatoms on aromatic pi–pi interactions: benzene–pyridine and pyridine dimer, J. Phys. Chem. A 113 (2009) 878–886.
[46] B.K. Mishra, N. Sathyamurthy, Pi–pi interaction in pyridine, J. Phys. Chem. A 109 (2005) 6–8.
[47] T.I. Oprea, G. Hummer, A.E. Garcia, Identification of a functional water channel in cytochrome P450 enzymes, Proc. Natl. Acad. Sci. U.S.A. 94 (1997) 2133–2138.
[48] D. Fishelovitch, S. Shaik, H.J. Wolfson, R. Nussinov, How does the reductase help to regulate the catalytic cycle of cytochrome P450 3A4 using the conserved water channel? J. Phys. Chem. B 114 (2010) 5964–5970.
[49] V. Cojocaru, P.J. Winn, R.C. Wade, The ins and outs of cytochrome P450s, Biochim. Biophys. Acta 1770 (2007) 390–401.
[50] Y. Zhao, W. Li, J. Zeng, G. Liu, Y. Tang, Insights into the interactions between HIV-1 integrase and human LEDGF/p75 by molecular dynamics simulation and free energy calculation, Proteins 72 (2008) 635–645.
[51] W. Li, Y. Tang, T. Hoshino, S. Neya, Molecular modeling of human cytochrome P450 2W1 and its interactions with substrates, J. Mol. Graph. Model. 28 (2009) 170–176.
[52] J.R. Jalas, S.S. Hecht, S.E. Murphy, Cytochrome P450 enzymes as catalysts of metabolism of 4-(methylnitrosamino)-1-(3-pyridyl)-1-butanone, a tobacco specific carcinogen, Chem. Res. Toxicol. 18 (2005) 95–110.
[53] W. Li, Y. Tang, H. Liu, J. Cheng, W. Zhu, H. Jiang, Probing ligand binding modes of human cytochrome P450 2J2 by homology modeling, molecular dynamics simulation, and flexible molecular docking, Proteins 71 (2008) 938–949.
[54] D.C. Haines, D.R. Tomchick, M. Machius, J.A. Peterson, Pivotal role of water in the mechanism of P450BM-3, Biochemistry 40 (2001) 13456–13465.
[55] M.R. Wester, E.F. Johnson, C. Marques-Soares, P.M. Dansette, D. Mansuy, C.D. Stout, Structure of a substrate complex of mammalian cytochrome P450 2C5 at 2.3 Å resolution: evidence for multiple substrate binding modes, Biochemistry 42 (2003) 6370–6379.